ADVANCED ENERGY MATERIALS

Supporting Information

for *Adv. Energy Mater.*, DOI: 10.1002/aenm.201200650

High Performance Thermoelectricity in Earth-Abundant Compounds Based on Natural Mineral Tetrahedrites

Xu Lu, Donald T. Morelli, Yi Xia, Fei Zhou, Vidvuds Ozolins, Hang Chi, Xiaoyuan Zhou, and Ctirad Uher*

Submitted to ADVANCED ENERGY MATERIALS

Supporting Information

for *Adv. Energy Mater.*, DOI: 10.1002/aenm.201200650

Title: High Performance Thermoelectricity in Earth-Abundant Compounds Based on Natural Mineral Tetrahedrites

Xu Lu, Donald T. Morelli*, Yi Xia, Fei Zhou, Vidvuds Ozolins, Hang Chi, Xiaoyuan Zhou, and Ctirad Uher
Email: dmorelli@egr.msu.edu

Materials and Methods

Tetrahedrite synthesis: $Cu_{12-x}(Fe,Zn)_{2-x}Sb_4S_{13}$ samples were synthesized by direct reaction of the starting elements- Cu(99.99 %, Alfa-Aesar), Sb(99.9999 %, Alfa-Aesar), and S, Zn, Fe (99.999%, Alfa-Aesar) . The elements were weighed out in stoichiometric proportions using a high-precision Mettler balance; typical charges were on the order of 5 grams total, with individual element masses weighed out with an accuracy of 0.0005 g (0.5 mg). The stoichiometric proportions of the elements were placed into quartz ampoules of inside diameter 10 mm and wall thickness 0.5 mm. The ampoules were evacuated of air using a turbo molecular pump; typical final pressures were $<10^{-5}$ Torr. The ampoules were sealed under dynamic vacuum using an oxygen/methane torch and provided with a small quartz hook on the top. A wire was attached to this hook and the ampoules were suspended in a vertical Thermolyne tube furnace at room temperature. The furnace was heated at 0.3 ºC min^{-1} to 650 ºC and held at that temperature for 12 hours. Subsequently, the furnace was cooled to room temperature at the rate of 0.4 ºC min^{-1}.

Natural tetrahedrite mineral: A natural specimen of tetrahedrite (photograph, **Figure S1**) was obtained from a mineral dealer[S1]. This specimen, which is identified as tetrahedrite from its geological characteristics, originated from Casapalca region of Peru. It also contained small regions of quartz (small white crystals, Figure S1), and pyrite (not shown in Figure S1).

As we describe below, this specimen is actually a solid solution of tetrahedrite ($Cu_{12}Sb_4S_{13}$) and tennantite ($Cu_{12}As_4S_{13}$).

Pellet consolidation: The reacted material was placed into a stainless steel vial and ball milled for five minutes in a SPEX sample preparation machine. These ball-milled powders were then cold pressed into a pellet and re-ampouled under vacuum for annealing for two weeks at 450 ºC. The final product after annealing was ball milled for 30 minutes into fine powders and hot-pressed under argon atmosphere at 80 MPa pressure and 430 ºC for 30 minutes. All the hot pressed samples used in this study were greater than 98% theoretical density, as measured using the Archimedes method. We synthesized two batches each of $Cu_{12-x}Zn_{2-x}Sb_4S_{13}$ and $Cu_{12-x}Fe_{2-x}Sb_4S_{13}$ samples. We would like to stress that *the high temperature thermoelectric property results presented in this article were all gathered from the same pellet for each of the compositions.* We also synthesized a pellet using the natural mineral as source material (designated sample N), and another pellet by mixing natural mineral powder with synthetic $Cu_{12}Sb_4S_{13}$ powder in a 1:1 weight ratio (designated sample N/S). These latter two samples were ball milled and hot-pressed using the same procedure as described above.

X-ray characterization: X-ray diffraction analysis of all of the synthesized specimens was performed by using a Rigaku Miniflex II bench-top X-ray diffractometer (Cu K_α radiation), and the results analyzed using a Jade software package. For each sample a small amount of hot-pressed material was powdered, spread on a microscope slide, and placed in the x-ray beam. **Figure S2** shows results of x-rays scans on representative $Cu_{12-x}Zn_{2-x}Sb_4S_{13}$ and $Cu_{12-x}Fe_{2-x}Sb_4S_{13}$ samples, respectively. All peaks index to the tetrahedrite crystal structure, and we see no evidence of any other phases in our samples. **Figure S3** displays the x-ray scan for sample N, the pure synthetic $Cu_{12}Sb_4S_{13}$, and for sample N/S. For the natural mineral sample N, we see peaks corresponding only to the tetrahedrite structure, but shifted to higher angle with respect to the synthetic $Cu_{12}Sb_4S_{13}$ sample. From electron microprobe

results (below) we conclude that this shift is due to the substantial amount of As on the Sb site in sample N. The x-ray scan for sample N/S also indicates that this sample is single phase and of the tetrahedrite crystal structure. The peaks are located midway between that of sample N and the pure $Cu_{12}Sb_4S_{13}$ sample, indicating that a solid solution has been formed during the hot pressing process.

Microprobe analysis of natural mineral: In order to determine the composition of the natural specimen, energy-dispersive X-ray electron spectroscopy (EDS) analysis was performed on several pieces of the sample previously identified as single phase tetrahedrite by x-ray diffraction. A representative result is shown in **Figure S4**. For the results shown here, if we scale the atomic constituents to a semimetal content of 4.00, the average composition of this portion of the mineral specimen is $Cu_{10.2}Fe_{1.4}As_{3.7}Sb_{0.3}S_{13.3}$. Across the series of sample regions probed, the composition deviated from that shown in Figure S4 by about 10 %. On the basis of these results, together with the x-ray analysis, we conclude that sample N, the natural tetrahedrite mineral, is a solid solution of tetrahedrite ($Cu_{12}Sb_4S_{13}$) and tennantite ($Cu_{12}As_4S_{13}$), with a Fe substitution level of approximately x = 1 – 1.5. On the basis of the x-ray results, Figure S3, we conclude that by mixing pure $Cu_{12}Sb_4S_{13}$ powder with powder from the natural crystal N, we can effectively "dilute" the Fe content in the sample. From the shift in the x-ray peaks we estimate that the composition of the diluted sample is approximately $Cu_{11.3}Fe_{0.7}Sb_{2.2}As_{1.8}S_{13}$. This puts this sample right in the range for optimal thermoelectric performance.

Thermal and electrical characterization: High temperature (373K-673K) Seebeck coefficient and electrical resistivity were measured in an Ulvac ZEM-3 system under argon. Typical specimen sizes for this measurement are 3x3x8 mm^3 with measurement performed along the long dimension. The thermal diffusivity (D) and heat capacity (C_p) from 373K to 673K were measured using the laser flash method (Netzsch, LFA 457) and differential scanning calorimetry (Netzsch, DSC200F3) respectively. The data were also confirmed

independently in a second laboratory using an Anter Flashline 5000 thermal diffusivity apparatus and a Netzsch 404C Pegasus calorimeter. Examples of data for heat capacity and thermal diffusivity are shown in **Figures S5 and S6**, respectively. The samples used for heat capacity and diffusivity measurements were from adjacent sections of the same pellets as those used for high temperature resistivity and Seebeck coefficient. The high temperature thermal conductivity was calculated using $\kappa = D * C_p * \text{density}$. Density measurements were performed using the Archimedes method with de-ionized water as the suspending fluid. We checked the Seebeck measurements by also measuring a bismuth telluride Seebeck standard sample (NIST SRM-3451), and found differences between our measurements and the calibration values of no more than 3 % over the range 300 – 573 K. The thermoelectric power factor for the Zn-substituted samples as well as that for specimens N and N/S are shown in **Figure S7.**

Theory details: Density-functional theory (DFT) calculations were performed with the projector-augmented wave (PAW) method as implemented in the highly efficient Vienna *Ab Initio* Simulation Package (VASP)[28]. Our self-consistent calculations used regular Monkhorst-Pack k-point meshes of 10 ×10×10 and a plane wave cutoff energy of 450 eV. The Perdew-Becke-Ernzerhof (PBE) exchange-correlation (xc) functional[30] was used to obtain the band structure shown in Figure 2; atom-decomposed electronic density-of-states over a wider energy range is shown in **Figure S8**. The calculated equilibrium lattice parameter was 10.403 Å, which compares well with the experimental value of 10.364 Å and presents a slight overestimation that is common for the PBE functional. To test the validity of the PBE functional, separate calculations were performed using the LDA+*U* method[31] with *U* values of 4 and 8 eV, as well as with the Heyd-Scuseria-Ernzerhof (HSE06) range-separated hybrid exchange functional[32]. The band structure near the Fermi level was found to be qualitatively unchanged w.r.t. the choice of the xc functional. Phonon dispersion curves were calculated using an in-house DFT linear response code. Optimized norm-conserving pseudopotentials

were generated for Cu $3d^{10}4s^1$, Sb $5s^25p^3$, and S $3s^23p^4$ valence configurations. Electronic wave functions were expanded in plane wave basis with a 680 Ry cutoff energy and the Brillouin zone was sampled on a regular 8 ×8×8 **k** point mesh. Dynamical matrices were calculated on a regular 2×2×2 **k** point grid and interatomic force constants were obtained via inverse Fourier transform; these force constants were then used to interpolate phonon dispersion throughout the Brillouin zone. Phonon mode Grüneisen parameters were obtained by taking finite differences between phonon frequencies calculated at two lattice parameters separated by 2%. These results were verified against the phonon frequencies calculated using the DFT force constant method on 236-atom supercells of $Cu_{12}Sb_4S_{13}$, obtained with the VASP code. Both methods produced phonon frequencies that were in excellent agreement with each other, typically differing by a only few per cent.

Zn- and Fe-substituted compounds. We investigated the energetics of Fe and Zn substitution on both the trigonal 12e and tetrahedral 12d sites; the tetrahedral sites were preferred by more than 0.4 eV per substitutional atom. The substitution sites for $Cu_{10}Zn_2Sb_4S_{13}$ were determined by picking the lowest-energy configuration among all symmetry-inequivalent substitutional pairs on the tetrahedral 12d sites. The calculated band structure of $Cu_{10}Zn_2Sb_4S_{13}$ is shown in **Figure S9**, showing that introduction of Zn leads to complete filling of the valence band states and semiconducting behavior. Spin-polarized band structure for $Cu_{11}FeSb_4S_{13}$ is shown in **Figure S10**. We find that the majority-spin e_g and t_{2g} states are approximately 3 eV below the valence band maximum (VBM), while the minority-spin states fall into the band gap just above the VBM, but below the conduction band states of $Cu_{12}Sb_4S_{13}$. This is happens due to exchange splitting between the Fe majority- and minority-spin states of approximately 3 eV. Fe is found to be in the s^0d^5 high-spin configuration, corresponding to the Fe^{3+} ionic state. Minority-spin e_g states lie just above the Fermi level and are slightly split due to deviations from perfect tetrahedral symmetry on the 12d sites.

Phonons of $Cu_{12}Sb_4S_{13}$: We calculated the energy versus phonon mode displacement curves for the unstable triply degenerate zone-center optical mode at *i*40 cm^{-1} in Figure 4. The resulting energy curve is shown in **Figure S11**, showing that this mode exhibits double-well structure with symmetrically placed minima at Cu displacements of approximately 0.3 Å away from the planar 12e sites. Full structural relaxation starting from the atomic configurations corresponding to these minima resulted in total energy lowering by 80 meV per formula unit, leading to a crystal structure with P1 symmetry. We hypothesize that significant structural disorder may be induced by freezing-in of those displacements at low temperatures, while at the same time leading to highly anharmonic vibrations and possible anharmonic stabilization of the cubic structure at high temperatures. The calculate phonon densities-of-states at two volumes (equilibrium volume and expanded by 6%) are shown in **Figure S12**. The unstable modes show strong frequency shifts towards harmonic stabilization upon increasing volume, manifesting in high Grüneisen parameters of more than 10 for the TA branches at zone boundaries (see Figure 4).

Reference

[S1]. Stefano Fine Minerals, Ann Arbor, Michigan, USA

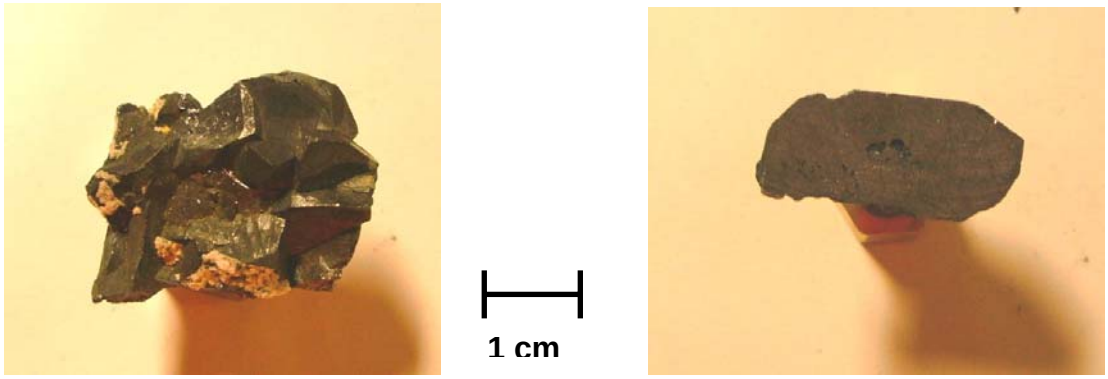

Figure S1. Photograph of a natural mineral specimen (left) identified geologically as tetrahedrite. The vast majority of the rock (dark grey regions) is tetrahedrite but inclusions of quartz (light colored regions) and pyrite (not shown) are also visible. The image at right shows a portion of the specimen in cross-section after cutting with a diamond saw.

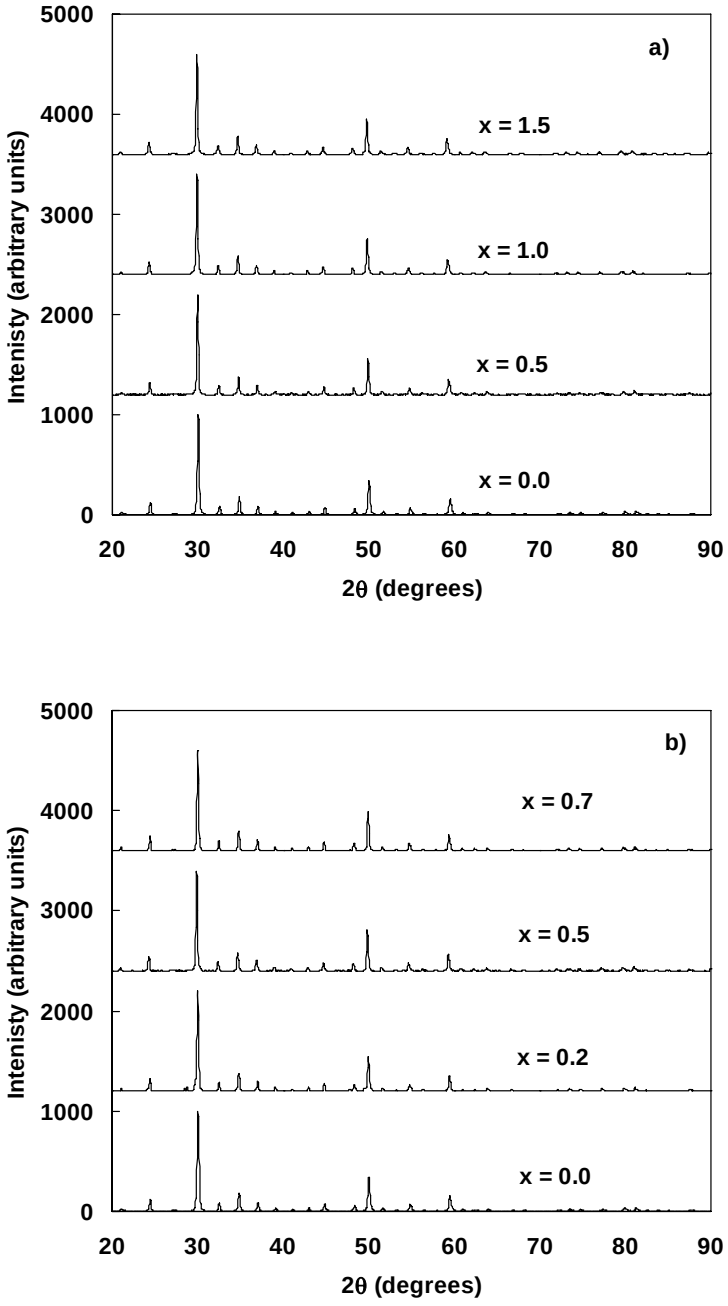

Figure S2. X-ray diffraction patterns for a) $Cu_{12-x}Zn_{2-x}Sb_4S_{13}$ and b) $Cu_{12-x}Fe_{2-x}Sb_4S_{13}$ samples. Also shown is an x-ray pattern for a natural mineral tetrahedrite specimen. All peaks index to the tetrahedrite phase, and no additional peaks due to second phases are detected.

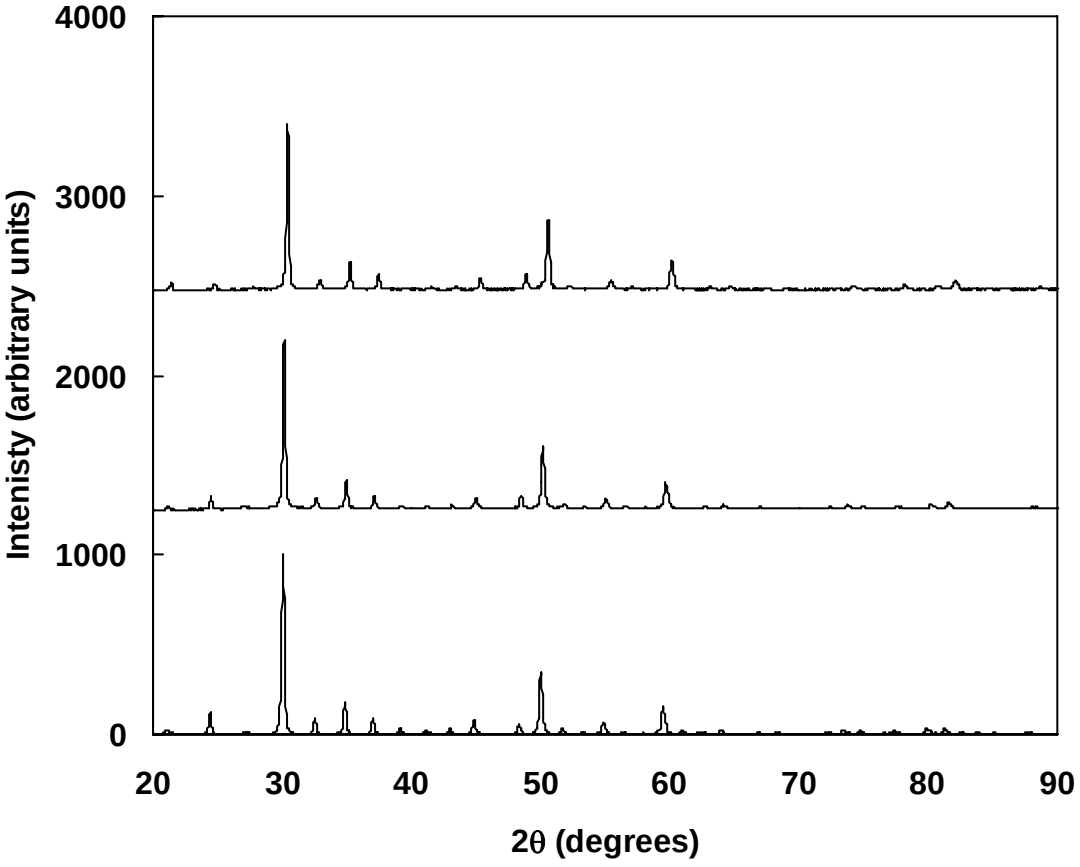

Figure S3. X-ray spectra of a pure synthetic $Cu_{12}Sb_4S_{13}$ (bottom), a pellet synthesized from natural mineral tetrahedrite/tennantite (sample N, top), and a pellet synthesized by mixing powders of the mineral and pure $Cu_4Sb_{12}S_{13}$ in a 1:1 weight ration and hot pressing (sample N/S, middle). Sample N/S is single phase tetrahedrite structure with x-ray peaks midway between that of the two precursor powders, indicating the formation of a solid solution.

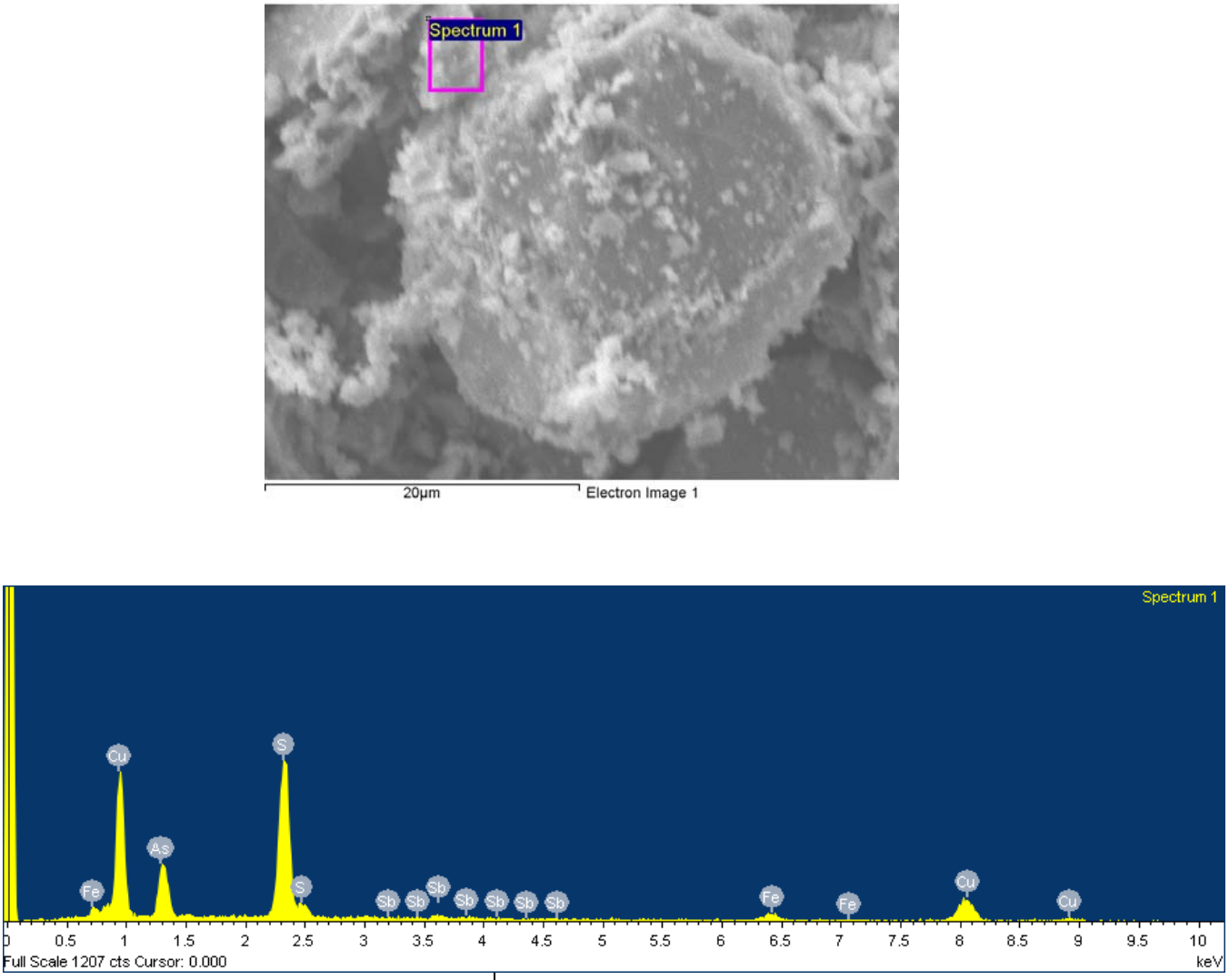

Totals	100.00

Figure S4. Representative result of energy-dispersive X-ray analysis of the natural specimen labeled N. Top: SEM image of region probed; middle: output spectrum from the microprobe; bottom: relative weight and atomic percentages of Cu, Fe, As, Sb, and S.

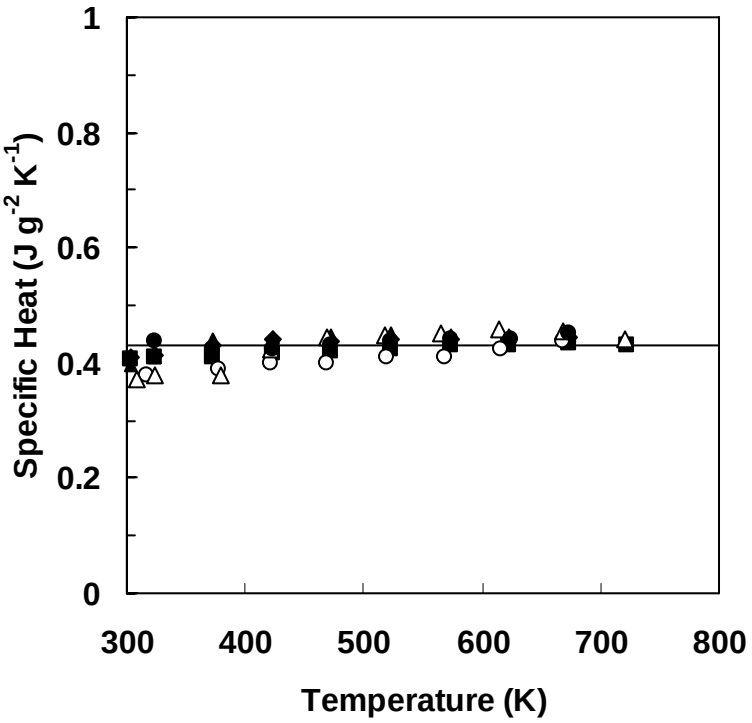

Figure S5. Specific heat capacity of Zn-substituted (solid circles: x = 0; solid squares: x = 0.5; solid triangles: x = 1.0; diamonds: x = 1.5) synthetic tetrahedrite specimens, sample N (open circles), a natural tetrahedrite specimen, and sample N/S (open triangles) synthesized from a mixture of the natural mineral powder and $Cu_{12}Sb_4S_{13}$ powder. The full line represents the Dulong-Petit value for $Cu_{12}Sb_4S_{13}$.

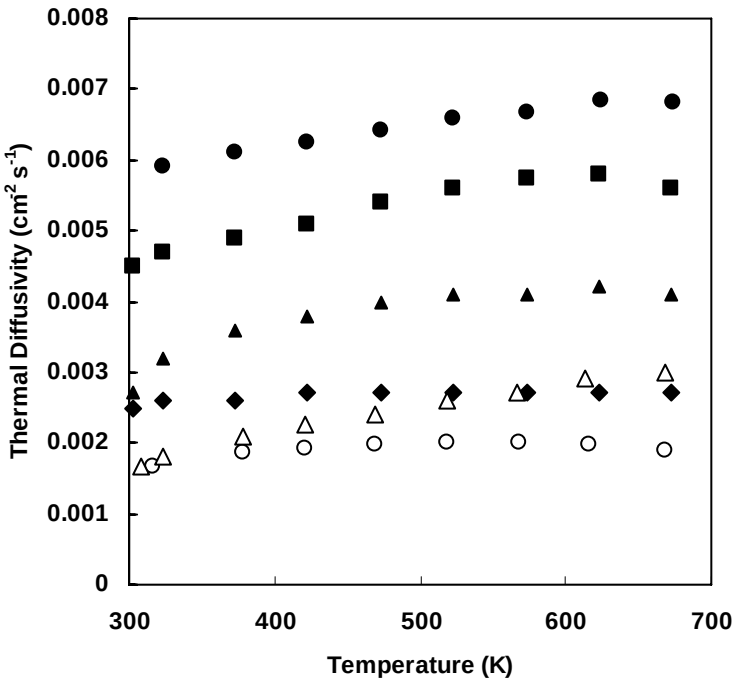

Figure S6. Thermal diffusivity of Zn-substituted (solid circles: x = 0; solid squares: x = 0.5; solid triangles: x = 1.0; diamonds: x = 1.5) synthetic tetrahedrite specimens, sample N (open circles), a natural tetrahedrite specimen, and sample N/S (open triangles) synthesized from a mixture of the natural mineral powder and $Cu_{12}Sb_4S_{13}$ powder.

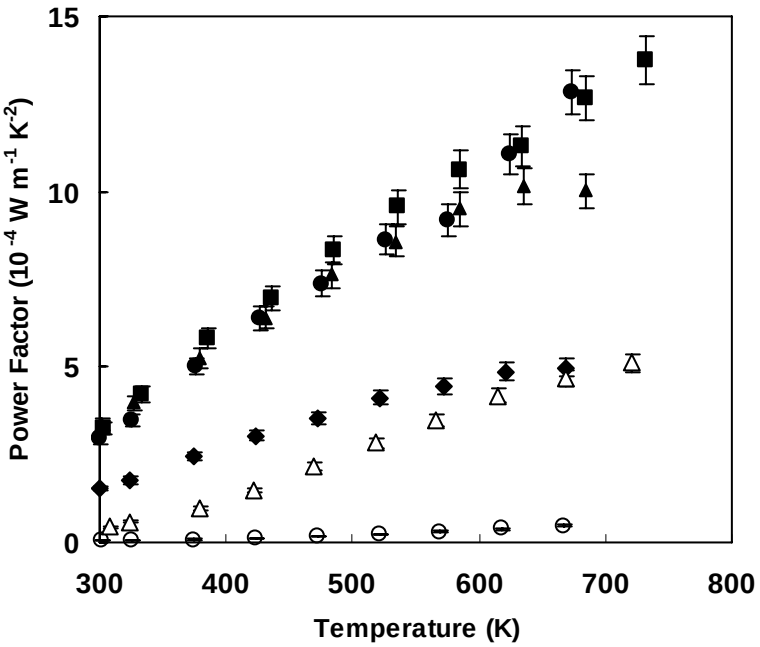

Figure S7. Thermoelectric power factor of Zn-substituted (circles, x = 0; squares, x = 0.5, triangles, x = 1.0, diamonds, x = 1.5) synthetic tetrahedrite. Also shown are the power factors of sample N (open circles), synthesized from the natural mineral specimen, and sample N/S(open triangles) synthesized from a mixture of the natural mineral powder and $Cu_{12}Sb4S_{13}$ powder..

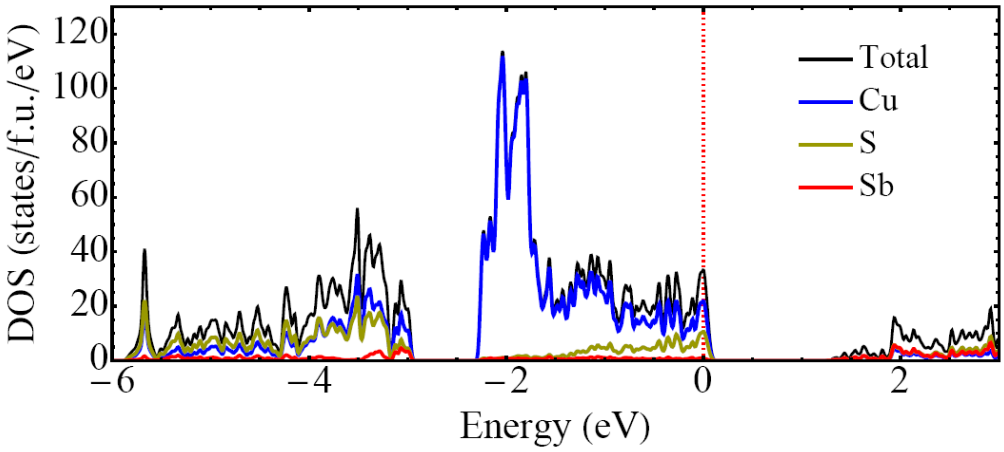

Figure S8. Calculated electronic band structure and density-of-states for $Cu_{12}Sb_4S_{13}$. The position of the Fermi level is denoted by a red dashed line.

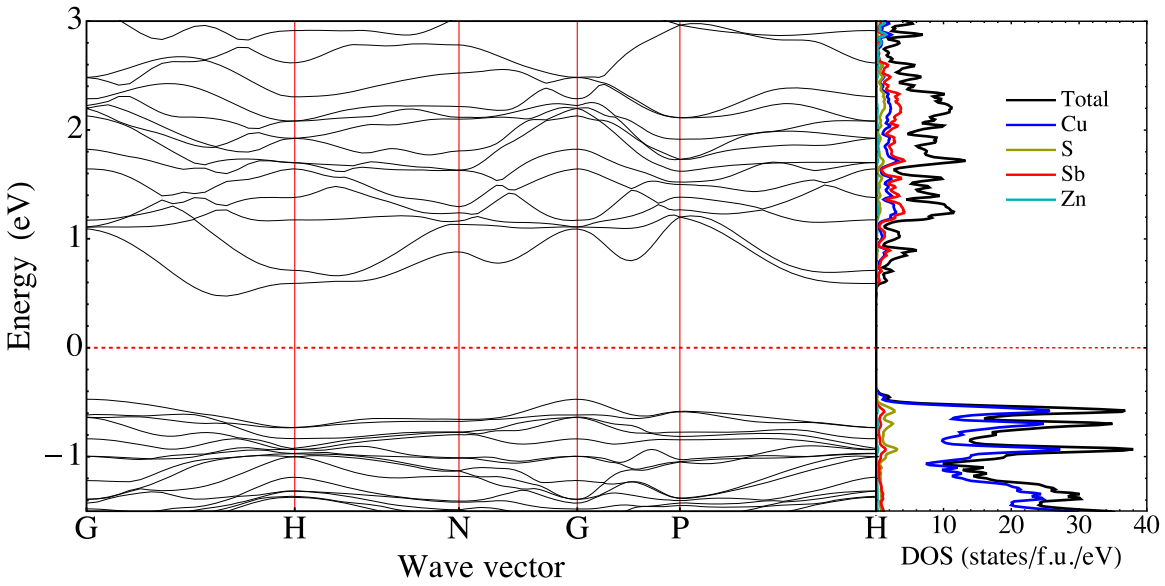

Figure S9. Calculated electronic band structure and density-of-states for $Cu_{10}Zn_2Sb_4S_{13}$. Zn atoms substitute on the tetrahedrally coordinated Cu sites and are found to be in the Zn^{2+} state. All the states in the valence band are fully filled and the Fermi level, marked by a dashed red line, falls in the middle of the band gap.

(a) Fe majority spin

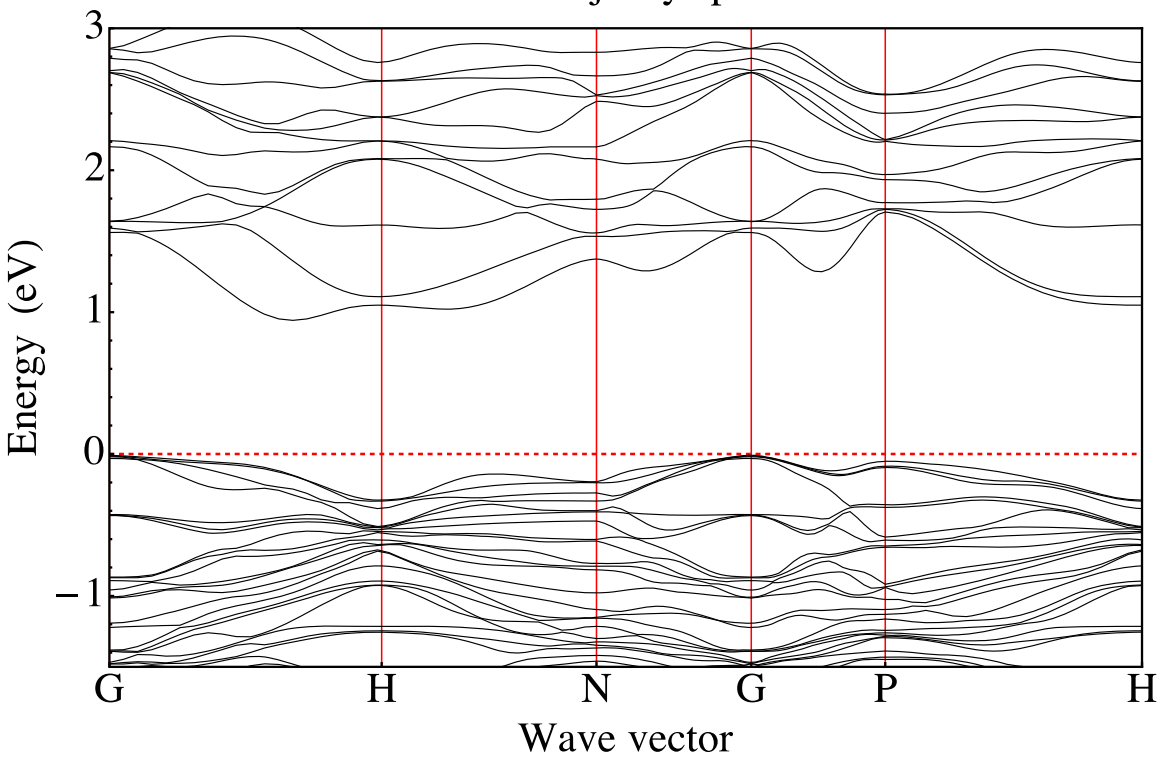

(b) Fe minority spin

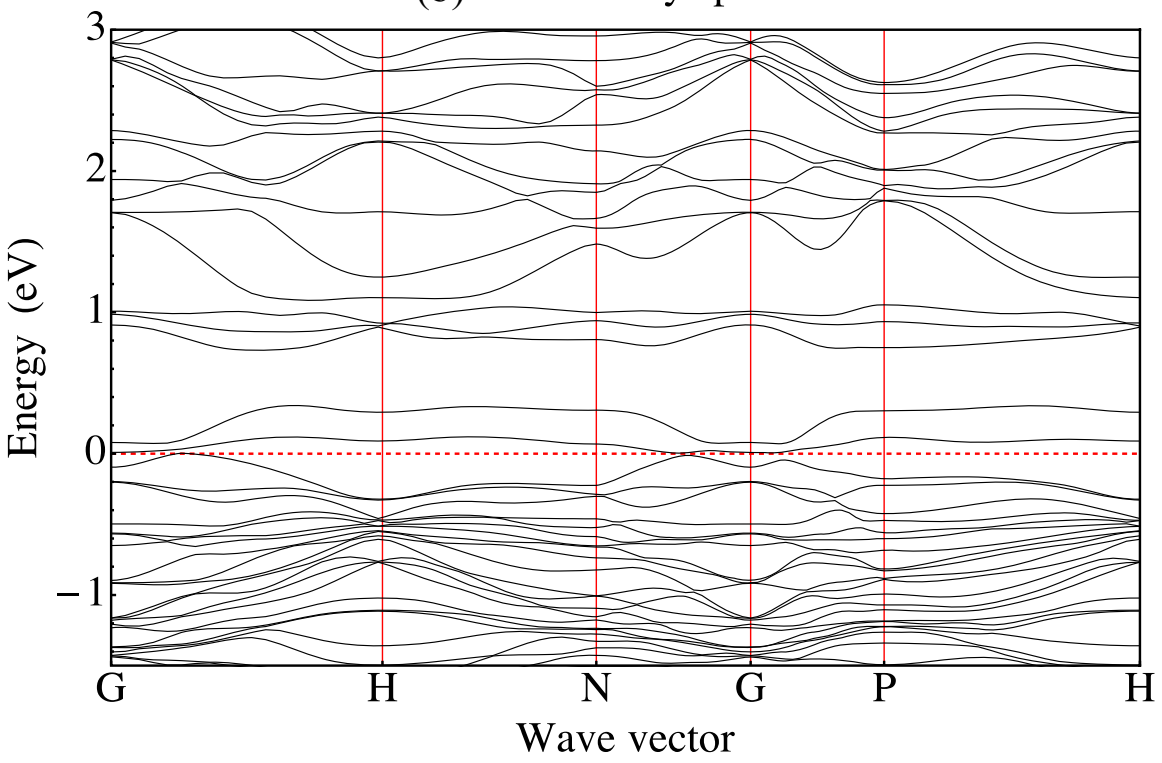

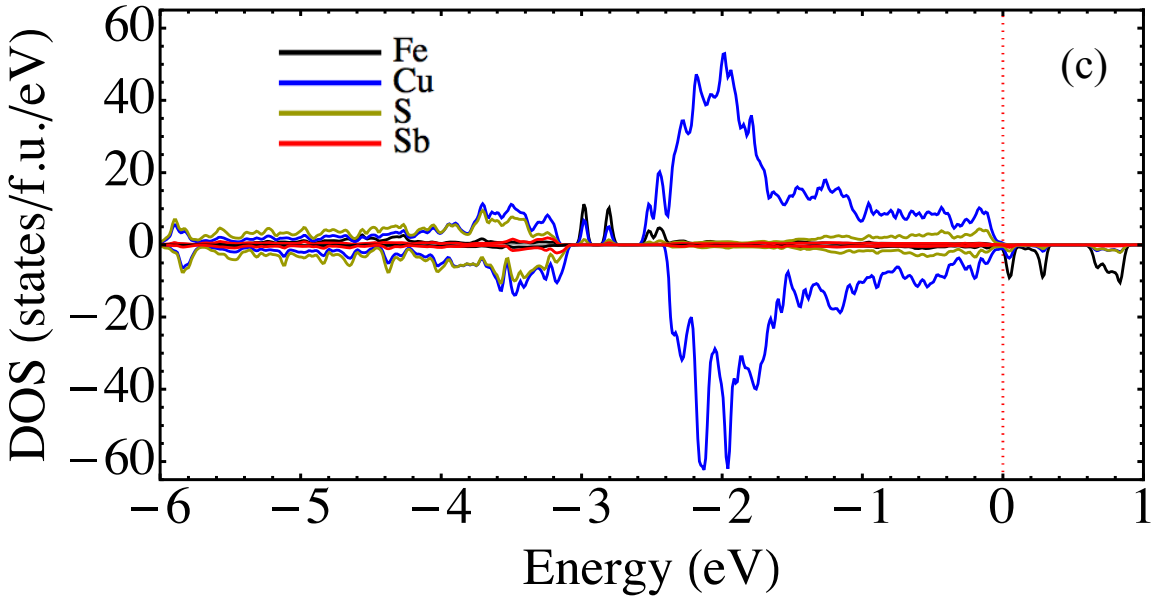

Figure S10. Calculated electronic band structure and density-of-states (DOS) for $Cu_{11}FeSb_4S_{13}$. Fe atom substitutes on a tetrahedrally coordinated Cu site. (a) Band dispersion for the majority spin states. (b) Band dispersion for the minority spin states. (c) Atom-decomposed electronic DOS. Majority-spin Fe e_g and t_{2g} states are, respectively, at approximately -3 and -2.5 eV relative to the Fermi level, which is shown as a dashed red line. The minority spin states are just above the Fermi level; e_g states are slightly split by crystal field effects due to deviations from tetrahedral symmetry on the Cu sites. Iron is found to be in the high-spin d^5 configuration of Fe^{3+}. Calculations were carried out using the exchange-correlation functional of Perdew, Becke, and Ernzerhof [Perdew, J. P., Burke, K., and Ernzerhof, M. Generalized Gradient Approximation Made Simple. *Physical Review Letters* 77, 3865-3868 (1996)].

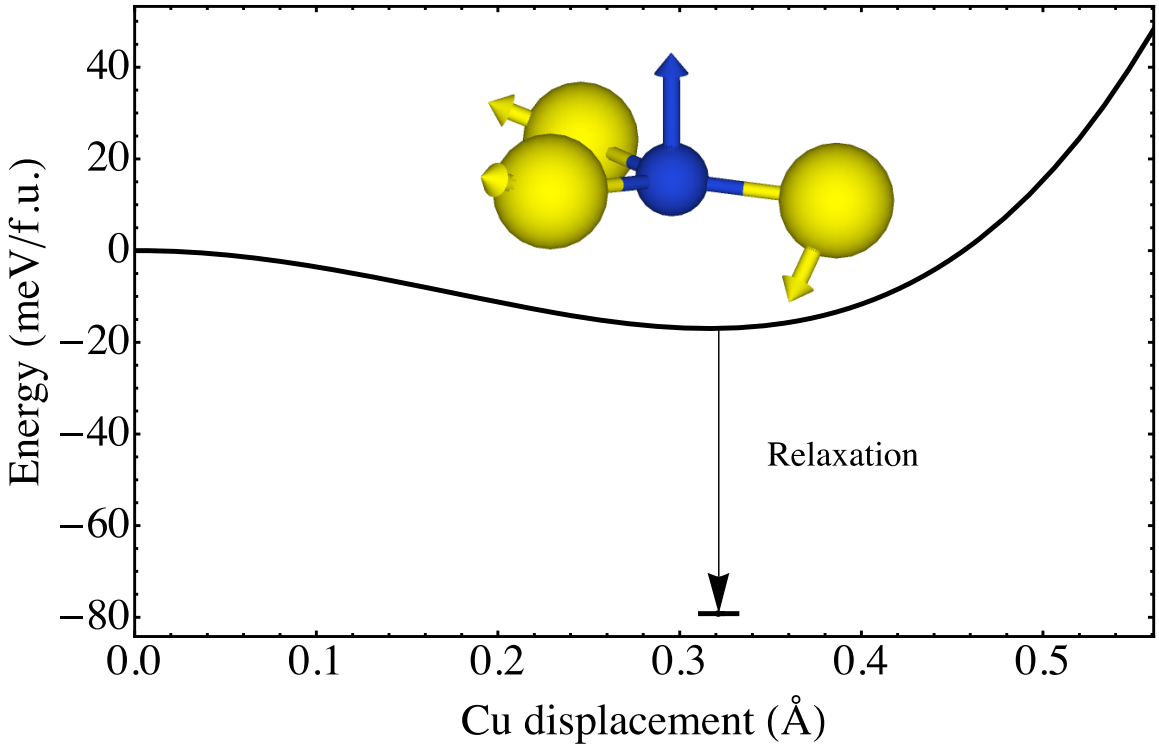

Figure S11. Total energy versus Cu displacement obtained by following the eigenvector of the unstable zone-center optical mode. Inset shows the pattern of atomic displacements for the three-fold coordinated Cu and its neighboring sulfur atoms. The arrow denotes the energy lowering obtained by fully relaxing all structural degrees of freedom starting with the atomic configuration at the minimum on the total energy versus displacement curve.

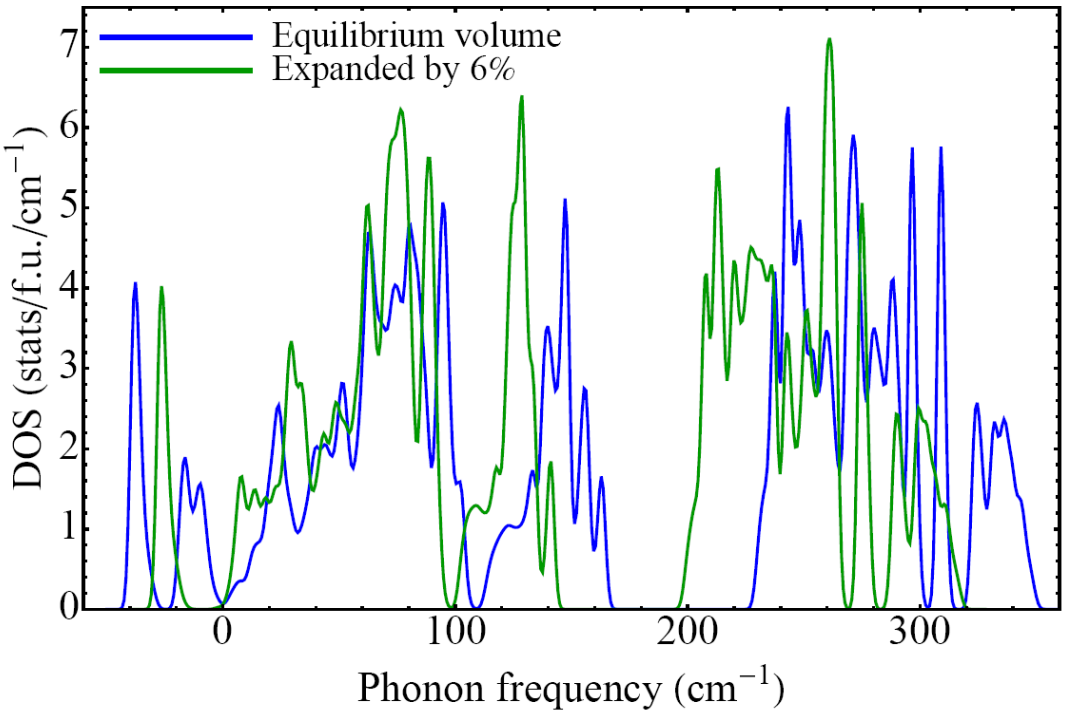

Figure S12. Calculated phonon density-of-states at the equilibrium volume V_0 (blue lines) and at $V=1.06\ V_0$ (green lines); harmonically unstable imaginary phonon frequencies are shown as negative values. It is seen that the unstable branches involving out-of-plane vibrations of the three-fold coordinated Cu atoms are stabilized by lattice expansion, while the higher-lying optical branches exhibit normal mode softening with increasing volume. Instabilities at the zone boundaries of the TA branches (double-peak structure at $i20$ cm^{-1}) are shifted to positive frequencies by 6% volume expansion.